Applied Thermal Engineering 225 (2023) 120154

Contents lists available at ScienceDirect

Applied Thermal Engineering

journal homepage: www.elsevier.com/locate/apthermeng

Research Paper

Thermal and electrical contact resistances of thermoelectric generator: Experimental study and artificial neural network modelling

Ying Li [a,b], Yong Shi [a,*], Xuehui Wang [b], Ding Luo [b], Yuying Yan [b,*]

[a] Department of Mechanical, Materials and Manufacturing Engineering, University of Nottingham Ningbo China, Ningbo 315100, China
[b] Fluids and Thermal Engineering Research Group, Faculty of Engineering, University of Nottingham, Nottingham NG7 2RD, UK

ARTICLE INFO

Keywords:
Thermoelectric generator
Thermal contact resistance
Electrical contact resistance
Performance assessment of thermoelectric generator
Artificial neural network

ABSTRACT

Thermal and electrical contact resistances (TCR and ECR) of thermoelectric generator (TEG) exert essential impacts on its performance. In this study, through a series of experiments these two important properties have been estimated in a wide range of thermal and mechanical conditions, and with different interfacial materials. The magnitudes of the overall TCR were found in the range of (1.12–2.00) $\times$ 10^{-3} $m^2 \cdot K/W$ with air, (0.82–1.81) $\times$ 10^{-3} $m^2 \cdot K/W$ with graphene sheet, and (3.61–8.37) $\times$ 10^{-4} $m^2 \cdot K/W$ with thermal grease as interfacial materials when the heat-source temperature varied from 348.15 K to 598.15 K and the imposed pressure load from 266 kPa to 1266 kPa. Importantly, the detailed TCRs at different locations across the TEG system were also analyzed. The dominant components, which occupy more than 80 % of the overall TCR, have been identified at the interfaces of the thermoelectric module contacting the heat source and heat sink. In our experiment, the corresponding ECRs under the same working conditions were (1.03–1.52) $\times$ 10^{-9} $\Omega \cdot m^2$, (0.56–9.60) $\times$ 10^{-10} $\Omega \cdot m^2$, and (1.05–6.23) $\times$ 10^{-10} $\Omega \cdot m^2$, respectively. Moreover, it is revealed that the TEG system delivered better performance at relatively low TCR and ECR when it operated at a high heat-source temperature, a large pressure load and using thermal grease as interfacial material. In addition to these experimental findings, a novel fully-connected feed-forward artificial neural network (ANN) model was also proposed to predict the overall TCR. It is shown that such an ANN model, as a promising approach, can achieve a cost-effective TCR prediction in good accuracy, with the mean square error and correlation coefficient being 2.36 $\times$ 10^{-9} and 99.4 %, respectively. These numerical and experimental results in this study will be of particular value for future TEG design and optimization.

1. Introduction

The last several decades have witnessed deteriorating global warming and air pollution caused by the large-scale consumption of fossil fuels. This poses grave challenges to the sustainable development of today's human society. Tremendous endeavors to reduce carbon emissions have been carried out, ranging from reshaping the energy consumption structure to developing advanced energy conversion technologies. Among various progress, thermoelectric generator (TEG) is one of the environmentally friendly and promising energy conversion (EC) devices, which directly obtains electricity under a temperature gradient based on the so-called Seebeck effect [1]. Such an EC device also has a simple structure and delivers reliable and noise-free performance. Due to these distinct advantages, TEG has been widely used in a large variety of engineering applications, including spaceship [2,3], wearable electronic equipment [4,5], ocean thermal energy harvest [6,7], solar energy capture [8-10], stove heat recovery [11,12], and automotive waste heat harvest [13,14].

To characterize the TEG performance, two important properties are introduced, i.e., the maximum conversion efficiency

$$\eta_{\max} = \frac{\sqrt{1+Z\overline{T}}-1}{\left(\sqrt{1+Z\overline{T}}+T_c/T_h\right)}\frac{\Delta T}{T_h} \tag{1}$$

and maximum power output

$$P_{max} = \frac{(S\Delta T)^2}{4R_\Omega^{TEM}} \tag{2}$$

where T_c and T_h are the temperatures on the cold and hot sides of the TEG module, and ΔT is their difference. $Z\overline{T}$, S and R_Ω^{TEM} represent the dimensionless figure of merit, Seebeck coefficient and electrical

* Corresponding authors.
E-mail addresses: Yong.Shi@nottingham.edu.cn (Y. Shi), Yuying.Yan@nottingham.ac.uk (Y. Yan).

https://doi.org/10.1016/j.applthermaleng.2023.120154
Received 14 September 2022; Received in revised form 4 January 2023; Accepted 30 January 2023
Available online 2 February 2023

Nomenclature

Symbols

A	cross sectional area (m^2)
$\mathbf{b}$	bias of the node
C_{cov}	covariance
f	activation function
h	height (m)
$\mathbf{I}$	unit matrix
$\mathbf{J}$	Jacobian matrix
L	distance (m)
N	number of TE couples
n	number of experimental data
P	power output (W)
P_L	pressure load (kPa)
q	heat transfer rate (W)
R	thermal resistance (K/W)
R_T	thermal contact resistance $(m^2\cdot K/W)$
δR_T	uncertainty of the overall TCR
R_E	electrical contact resistance $(\Omega\cdot m^2)$
δR_E	uncertainty of the ECR
R_Ω	electrical resistance (Ω)
r	correlation coefficient (%)
S	Seebeck coefficient
T	temperature (K)
ΔT	temperature difference upon TEG (K)
ΔT_0	temperature difference upon TE legs (K)
V_{oc}	open-circuit voltage
$\mathbf{w}$	weight of the node
$\mathbf{x}$	input of the node
$\mathbf{y}$	output
$\mathbf{y}_{pre}$	predicted data
$\mathbf{y}_{exp}$	experimental data

Greek symbols

η	conversion efficiency (%)
λ	thermal conductivity $(W/(m\cdot K))$
μ	positive constant in Eq. (24)
ρ	electrical resistivity $(\Omega\cdot m)$
σ	electrical conductivity (S/m)

Acronyms

ANN	artificial neural network
AAD	average absolute deviation (%)
ECR	electrical contact resistance $(\Omega\cdot m^2)$
MSE	mean square error
RD	relative deviation (%)
TCR	thermal contact resistance $(m^2\cdot K/W)$
TE	thermoelectric
TEG	thermoelectric generator
$Z\overline{T}$	dimensionless figure of merit

Subscripts

a	air
al	aluminium block

Superscripts

c	cold side on the surface of heat sink
ce	ceramic
el	copper electrodes
gs_V	vertical direction of graphene sheet
gs_H	horizontal direction of graphene sheet
h	hot side on the top surface of aluminium block
ht	heat source
i	i^{th} component
I	layer I
II	layer II
III	layer III
leg	TE legs
max	maximum
n	n-type TE material
p	p-type TE material
tg	thermal grease
w	water bath
c	cold side on the surface of heat sink
e	external
el	copper electrodes
h	hot side on the top surface of aluminium block
i	internal
leg	TE legs

resistance of the TEG module [15,16]. Equations (1) and (2) indicate that high values of $Z\overline{T}$ and ΔT will lead to high η_{max} and a large P_{max}, thus directing to better TEG performance. In line with this understanding, immense efforts, including doping [17,18], alloys [19,20] and nanostructures [21], have been made in the literature in fabricating novel TE materials at large $Z\overline{T}$. Meanwhile, considerable attention was also paid to establishing or maintaining a large temperature difference between the hot and cold sides of the TEG module, ΔT. For example, Refs. [14,22] have proposed some interesting designs integrating high-efficiency heat pipes into the TEG systems. Ref. [23] studied a TEG system utilizing heat exchangers between the heat reservoir and TEG module. To be rigorous, the TEG performance is of direct relevance to the temperature difference upon the TE legs, ΔT_0, rather than ΔT. In practice, the former is actually lower than the latter due to the existence of thermal contact resistance (TCR) among different components of the TEG [24]. Therefore, a large ΔT does not always mean a large ΔT_0, and would not necessarily lead to high TEG performance if the TEG system suffers from significant TCR. Refs.[25,26] theoretically analyzed an annular thermoelectric couple, and found that the inclusion of TCR resulted in a reduced ΔT_0 and thus a smaller P_{max} and lower η_{max} in comparison to the case ignoring TCR. Furthermore, the results in Ref. [27] revealed that there was a discrepancy of 28.8 % in P_{max} between the TEGs with and without TCR being considered. It is worth pointing out that TCR often deteriorates the TEG performance along with electrical contact resistance (ECR) between copper electrodes and TE legs in the TEG. Still in Ref. [27], it is found that in the case with the leg length $l = 3.2$ mm, the P_{max} of the TEG dropped by 18 % when both TCR and ECR were included. When the leg length shrank to $l = 0.2$ mm, the reduction in P_{max} jumped to 90 %. In addition, the results with TCR and ECR also showed the optimal length of TE legs was much longer than their counterparts without TCR and ECR effects [26,28].

All the aforementioned studies have indicated that an accurate TEG design and its performance assessment necessitate definite estimations of TCR and ECR in the system. For TCR of a TEG, there are three main methods in the literature to estimate its value. The first one is based on its definition, i.e.,$R_T = (\Delta T/q)A$, where ΔT and q represent the temperature difference and heat transfer rate across the interface between two contacting surfaces. A is the interfacial area. It makes use of temperature measurements and thermal properties of the used materials to specify ΔT and q. This method was widely used in today's TCR estimation [29-31]. Sakamoto *et al.* [29] carried out experiments based on this method to estimate TCR of TEGs with different thermal interfacial materials (Whity Paint, PF20-G3, TC-50TXS, TSU700-H, and SC102) in a

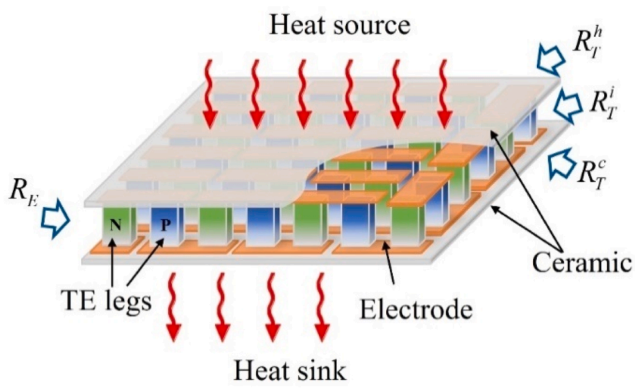

Fig. 1. Schematic of a TEG system with its ECR and TCRs at different locations.

temperature range of 600–900 K. In their study, the values of TCR were as low as 5.8×10^{-5} m^2·K/W and 5.7×10^{-5} m^2·K/W, respectively, when Whity Paint and TSU700-H were employed. Also, Wang *et al.* [30] estimated the overall TCR of their TEG using the same method, and obtained their TCR in the range of 8.06×10^{-4} –1.33×10^{-3} m^2·K/W under different pressure loads. As to the second method, it follows the same thought to estimate TCR based on its definition; however, the heat transfer rate and temperature difference through the contacting surfaces are obtained by taking the advantage of the instantaneous response difference between the electric field and temperature field when the TEG shifts from its open-circuit mode to its closed-circuit mode. [32,33]. With this method, Buchalik *et al.* [32] estimated the total TCR of their TEG ranging from 3.14×10^{-4} m^2·K/W to 6.59×10^{-4} m^2·K/W. Pitarch *et al.* [33] specified the external TCR on the hot and cold sides of a commercial TEG module at 3.57×10^{-4} m^2·K/W when the interfacial material was thermal grease. The third method to estimate TCR is through use of electrical impedance spectroscopy. For example, Pitarch *et al.* [34] used this method to evaluate the internal TCR between the copper electrodes and ceramic layers, and obtained its magnitudes ranging from 2.2×10^{-6} to 1.26×10^{-5} m^2·K/W at the room temperature. As for ECR in TEG, although important, very limited work has been carried out. Ref. [35] proposed a scanning probe method to estimate the ECR of a TE leg, and successfully obtained that it was approximately equal to 7×10^{-10} Ω·m^2. So far, all these aforementioned publications focus on either TCR or ECR. They do not provide comprehensive estimations of both TCR and ECR in their TEG systems. Moreover, a detailed understanding of TCRs at different locations in a TEG is unavailable yet.

In this study, we tackle these issues through a series of experiments on a TEG system operating in a large variety of working conditions. We investigate the dependence of the relevant TCR and ECR at different heat-source temperatures, pressure loads and interfacial materials. Importantly, we evaluate the magnitudes of TCR components at different locations and identify the major contribution to the overall TCR of the TEG. These results provide rich and valuable references for

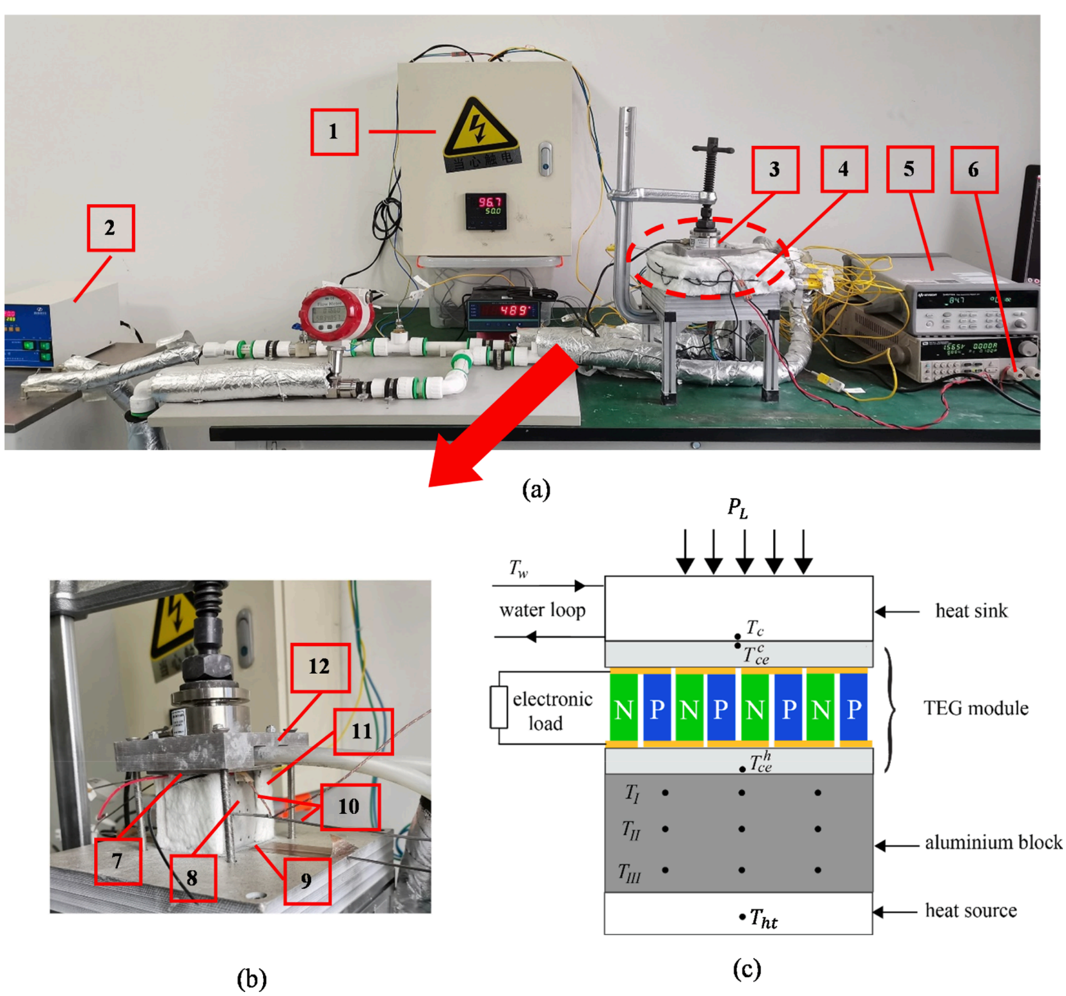

Fig. 2. The experimental setup of the TEG system. (a) front view; (b) enlarged view of the TEG rig; (c) schematic of the TEG rig with temperature measurement points. 1–power supply, 2–water bath, 3–pressure sensor, 4–TEG rig, 5–data logger, 6–electronic load, 7–TEG module, 8–aluminium block, 9–alumina ceramic heater (heat source), 10–thermocouples, 11–aerogel blanket, 12–heat sink.

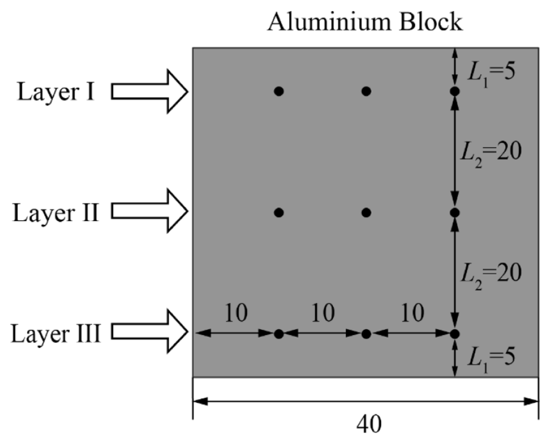

Fig. 3. Temperature measurement points in the aluminium block.

future TEG design and its performance optimization. Besides these experimental studies, a novel and efficient artificial neural network model is also proposed for TCR prediction in this study. Through its numerical simulations, we demonstrate it as a promising and cost-effective approach for TCR prediction in future TEG applications.

The rest of the study is organized as follows: The experimental setup, test methodology, thermal and electric analyses on TCR and ECR estimation, and uncertainty analysis on experimental measurements are presented in Section 2. In Section 3, we elaborate the TCRs at different locations and the ECR variations of a TEG system operating in a wide range of heat-source temperatures and pressure loads, and using three different interfacial materials. The corresponding TEG performance is also discussed in this section. In Section 4, an ANN model based on the experimental data is proposed, and its accuracy and effectiveness for TCR prediction are examined. Finally, the conclusions are summarized in Section 5.

2. Experiment for TCR and ECR estimation

In this section, a TEG system is built up and a series of experiments are conducted to estimate its TCR and ECR. In particular, the overall TCR of the TEG is decomposed into the external and internal components, i.e., R_T^e and R_T^i. The former includes the TCR at the interface between the heat source and the hot side of the TEG, R_T^h, and its counterpart between the heat sink and the cold side, R_T^c. For R_T^i, it consists of the TCRs among ceramics, copper electrodes and TE legs, as shown in Fig. 1. As to the ECR, R_E, it exists between copper electrodes and TE legs. This property, together with the aforementioned TCRs, is evaluated in our experiments based on the real-time and onsite measurements of the voltage, current and temperatures at different locations of the TEG setup.

2.1. Experimental setup and test methodology

2.1.1. Experimental setup

Fig. 2 shows the experimental setup in this study. It contains a power supply, a thermostatic water bath, a heat sink, a pressure controller, a TEG module, an electronic load, and a data logger. The power supply was used to provide heat to an MCH alumina ceramic heating sheet, which played a role as the heat source in experiment. Its temperature was modulated by a built-in PID controller. The TEG module in use was TEG1-12708 (Sageron, China) with 127 pairs of TE legs. Its heat was taken away by a water loop from a thermostatic water bath (Blue Instrument Technology, China). To better estimate the heat transfer rate towards this TEG module, an aluminium block (AL 6061-T6) was inserted between it and the heat source. This block, together with the TEG module, was covered by an aerogel blanket. Moreover, the TEG module was connected with an external electronic load (IT8513A+, Itech, USA), by which its output voltage, current and power were recorded. In experiment, all pressure loads imposed on the TEG setup were measured and regulated by a pressure sensor (JHBM-H1, Zhongwan Jinnuo, China, with accuracy of 0.49 N) and a pressure controller.

To gain in-situ temperature measurements, 12 thermal couples were allocated across the TEG setup, as shown in Fig. 2(c). To be specific, two adhesive fast response surface thermocouples (SA1XL-K-SRTC, Omega, USA) were attached on the hot and cold ceramic surfaces of the TEG module, respectively, while another (SCAIN-062U-6-SHX, Omega, USA) was inserted into the bottom surface of the heat sink. To estimate the heat transfer rate from the heat source to the TEG module, the other thermocouples (SCAIN-062U-6-SHX, Omega, USA) were inserted into nine cavities (each with a depth of 20 mm) evenly distributed into three layers along the aluminium block, as shown in Fig. 3. The accuracy of all thermocouples has been calibrated within $\pm 0.1\ ^\circ C$, and their measurements were collected by a data logger (34970A, Keysight, USA). It is also worth mentioning that the voltage and the current recorded by the electronic load have a resolution of 0.1 mV and 0.1 mA, respectively.

In experiment, two interfacial materials, i.e., graphene sheet (Zhixian Rexinxi, China) and thermal grease (VK-887, Weiyujk, China), were employed at both the hot and cold sides of the TEG module. The former is chosen because it has extra high thermal conductivity in the horizontal and vertical directions, while the latter is one of the most commonly used thermal interfacial materials in the current TEG applications. For graphene sheet, its working temperature ranges from

Table 1
The properties of the used materials and the geometries of different components in the TEG setup.

Components	Materials	Properties	Geometry (L × W × H) mm
Interfacial materials	air	$\lambda_a = 0.024$	—
	graphene sheet	$\lambda_{gs\_V} = 100$ $\lambda_{gs\_H} = 2500$	40 × 40 × 0.05
	thermal grease	$\lambda_{tg} = 6$	—
Aluminium block	AL6061−T6	$\lambda_{al} = 156$[36]	40 × 40 × 50
Electrodes	copper	$\lambda_{el} = 398$[37] $\rho_{el} = 1.851 \times 10^{-8}$	3.8 × 1.4 × 0.4
Ceramic layer	Alumina ceramic (96 %)	$\lambda_{ce}(T) = -0.02857T + 28.37571$ [38]	40 × 40 × 0.7
P-type leg	Bi_2Te_3-based	$\lambda_p(T) = -6.8387 + 0.06974T - 1.89493 \times 10^{-4}T^2 + 1.68484 \times 10^{-7}T^3$ $\rho_p(T) = (0.66477 - 0.00425T + 1.63796 \times 10^{-5}T^2 - 9.03496 \times 10^{-9}T^3) \times 10^{-5}$	1.4 × 1.4 × 1.6
N-type leg	Bi_2Te_3-based	$\lambda_n(T) = -5.0958 + 0.05713T - 1.59031 \times 10^{-4}T^2 + 1.47351 \times 10^{-7}T^3$ $\rho_n(T) = (-3.40847 + 0.02591T - 5.52879 \times 10^{-5}T^2 + 4.45197 \times 10^{-8}T^3) \times 10^{-5}$	1.4 × 1.4 × 1.6

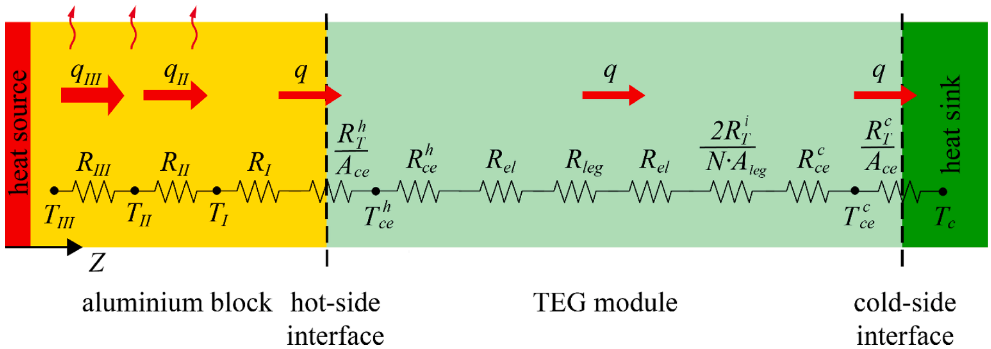

Fig. 4. Schematic of the equivalent circuit of thermal resistances in the TEG system.

223.15 K to 723.15 K, while thermal grease can work well from 213.15 K to 673.15 K. Note that our experiments also included the cases having two surfaces in direct contact without any interfacial materials but air. For convenience, such a working circumstance is denoted as "using air as interfacial material" hereafter, and it will be used as a reference to highlight the effects of graphene sheet and thermal grease on TCR and ECR. Table 1 summarizes the properties of the used materials and the geometries of different components in our TEG setup. The physical meaning of each symbol and its unit have been given in the Nomenclature.

2.1.2. Test methodology

In this study, the TEG module was operated in its open-circuit mode for its TCR estimation. To be specific, the pressure load in each TCR experiment was first imposed on the TEG module using the clamping device (pressure controller). The heat source was then turned on, with its temperatur increasing up to the pre-set value. Meanwhile, the temperature in the water bath was set to be 293.15 K. During this process, the temperature measurements were recorded only after their fluctuations had been lower than 0.1 °C for 30 minutes. Under this circumstance, a thermal equilibrium was reached in the system. Note that once all the measured temperatures were specified, the TCR was calculated based on the model introduced in Section 2.2, together with the material properies and component geometries given by Table 1. As to ECR estimation, the TEG module was connected with an external electronic load (IT8513A+, Itech, USA), whose value decreased from 10 Ω to 0.1 °C at an interval of 0.1 °C with each step lasting for 10 seconds. This electronic load also recorded the voltage and current of the TEG module under different external load resistances, and a U-I curve was obtained. The absolute value of this curve slope was the overall electrical resistance of the TEG module, R_{Ω}^{TEM}. Again, with this result, together with the material properties and component geometries in Table 1, the ECR was specified based on the model in Section 2.2.

2.2. Analysis for TCR and ECR estimation

In Section 2.1, we introduced the TEG experimental setup and test methodology in this study. Next, we analyze heat transfer and electric conduction in such a TEG system, and derive its TCR and ECR based on the experimental measurements. We first focus on the TCR, R_T, defined as

$$R_T = (\Delta T/q)A \tag{3}$$

where ΔT and q represent the temperature difference and heat transfer rate across the interface between two contacting surfaces. A is the corresponding interfacial area. In this study, the heat transfer from the heat source to the heat sink is modelled by an equivalent circuit with thermal resistances in series. As shown in Fig. 4, all the TCRs and thermal resistances at different locations, together with the related temperature measurements, are marked. Note that to exclude the effects resulting from the Peltier heat and Joule heat, the temperature measurements in these TCR experiments were conducted in the open-circuit mode of the TEG module.

It is seen in Fig. 4 that the equivalent circuit includes the thermal resistances, R_{III}, R_{II}, R_I, R_{ce}^h, R_{ce}^c, R_{el} and R_{leg}. The first three represent the thermal resistances in the aluminium block between Layer III and Layer II, Layer II and Layer I, Layer I and the interface of the block contacting the TEG module; R_{ce}^h and R_{ce}^c are the ceramic thermal resistances in the hot and cold sides of the TEG module; R_{el} and R_{leg} are the thermal resistances of the copper electrodes and TE legs, respectively. Generally, these thermal resistances except R_{leg} are specified by

$$R_i = \frac{h_i}{\lambda_i A_i} \tag{4}$$

where h_i, λ_i and A_i denote the thickness, thermal conductivity and cross-sectional area of the component, i. As to R_{leg}, it is computed by

$$R_{leg} = \frac{h_{leg}}{N\left[\lambda_p(T) + \lambda_n(T)\right]A_{leg}} \tag{5}$$

h_{leg} is the TE leg height. A_{leg} and N are the corresponding cross-sectional area and the number of TE couples in the TEG module. In Eq. (5), R_{leg} also relies on two temperature-dependent thermal conductivity, $\lambda_p(T)$ and $\lambda_n(T)$. Both are determined by the average temperature of the TE legs in the hot and cold sides, i.e.,

$$T = \frac{T_{leg}^h + T_{leg}^c}{2} = \frac{\left[T_{ce}^h - q\left(R_{ce}^h + R_{el}\right)\right] + \left[T_{ce}^h + q\left(R_{ce}^c + R_{el}\right)\right]}{2} \tag{6}$$

where T_{leg}^h and T_{leg}^c are the leg temperatures on its hot and cold sides. It should be pointed out that we did not measure these two temperatures but those on the ceramic layers (i.e., T_{ce}^h and T_{ce}^c) in the experiments. Therefore, the value of T was indeed specified by the right-hand side of the second equality of Eq. (6).

As to TCR, it includes an internal component in the TEG module, R_T^i, and two external components at the interfaces of the TEG module with the aluminium block and heat sink, i.e., R_T^h and R_T^c, respectively. To evaluate their values, we analyze the heat transfer processes in the aluminium block, TEG module and across their interfaces. Note that these components were covered by an aerogel blanket during the experiments. Moreover, the TEG module was rather thin—its thickness was just 3.8 mm. Under these experimental conditions, the heat loss of the TEG module to the surroudings was negligibly small. As a result, the heat transfer from the hot-side interface, throughout the TEG module, to the cold-side interfaces is one-dimensional heat conduction with thermal resistances in series. Its heat transfer rate,q, is a constant and can be calculated in terms of the temperature differences of $T_I - T_{ce}^h$, $T_{ce}^h - T_{ce}^c$ and $T_{ce}^c - T_c$, respectively, subject to the Fourier law. It follows that

Process $(T_I \rightarrow T_{ce}^h)$:

Table 2
Uncertainty of each measurement.

Measurements	Uncertainty
Temperature (after calibration)	0.1 °C
Voltage	0.1 mV
Current	0.1 mA

$$q = \frac{T_I - T_{ce}^h}{R_I + R_T^h / A_{ce}} \tag{7a}$$

Process $(T_{ce}^h \rightarrow T_{ce}^c)$:

$$q = \frac{T_{ce}^h - T_{ce}^c}{R_{ce}^h + R_{ce}^c + 2R_{el} + R_{leg} + 2R_T^i/(N \cdot A_{el})} \tag{7b}$$

Process $(T_{ce}^c \rightarrow T_c)$:

$$q = \frac{T_{ce}^c - T_c}{R_T^c / A_{ce}} \tag{7c}$$

As to the anluminium block, although it was also wrapped by the aerogel blanket, it was 12 times thicker than the TEG module. To be precise, we do not simply ignore its heat loss to the surroundings, but assume such heat loss is evenly dissipated along the aluminium block (i.e., in the Z direction in Fig. 4). This gives rise to a linear decreasing heat transfer rate through the aluminium block,

$$\frac{q_{III} - q_{II}}{q_{II} - q} = \frac{L_2}{0.5L_2 + L_1} \tag{8}$$

where q_{II} and q_{III} represent the heat transfer rates along the Z direction between Layer I and II, and between Layer II and III. L_1 and L_2 are the distances among these layers, as shown in Fig. 3. Expressing q_{II} and q_{III} in terms of T_I,T_{II} and T_{III} (the average temperatures at Layer I, II and III) based on the Fourier law yields

$$q = q_{II} - \frac{0.5L_2 + L_1}{L_2}(q_{III} - q_{II}) = \frac{7}{4}\left(\frac{T_{II} - T_I}{R_{II}}\right) - \frac{3}{4}\left(\frac{T_{III} - T_{II}}{R_{III}}\right) \tag{9}$$

Combining Eqs. (4)–(9) leads to the external TCR and internal TCR of the TEG module

$$R_T^h = \frac{T_I - T_{ce}^h}{q/A_{ce}} - R_I A_{ce} \tag{10}$$

$$R_T^c = \frac{T_{ce}^c - T_c}{q/A_{ce}} \tag{11}$$

$$R_T^i = \frac{1}{2}\left(\frac{T_{ce}^h - T_{ce}^c}{q/(NA_{el})} - \left(R_{ce}^h + R_{ce}^c + 2R_{el} + R_{leg}\right)NA_{el}\right) \tag{12}$$

The overall TCR of the whole TEG system, $R_T = R_T^h + R_T^c + R_T^i = R_T^e + R_T^i$, with R_T^e being the total external TCR.

Our second interest is to estimate the ECR of the TEG setup. Generally speaking, this property is defined as the electrical resistance at the contacting interface per unit area. It occurs at the interfaces between the copper electrodes and TE legs on both the hot and cold sides. From the experimental perspective, it is challenging to directly measure the ECR in the current conditions. Althernatively, an indirect way is proposed—we conduct an experiment to measure the overall electrical resistance of the whole TEG module, R_Ω^{TEM}, and then specify the intrinsic electrical resistances of the TE legs and copper electrodes, i.e., R_Ω^{leg} and R_Ω^{el}. The difference between R_Ω^{TEM} and these two intrinsic electrical resistances (R_Ω^{leg} and R_Ω^{el}) will give rise to the ECR of the TEG setup. In line with this thought, an electronic load was electrically connected with the TEG module in series, and worked in its constant resistance mode. Under the closed-circuit circumstance, the electronic load delivered its currents and voltages at various heat-source temperatures and pressure loads, when different interfacial materials were used. Curve fitting of these electrical signals led to the overall electrical resistance of the TEG module, R_Ω^{TEM} (see the details in the appendix). As to R_Ω^{leg} and R_Ω^{el}, they are specified by

$$R_\Omega^{leg} = \frac{N \cdot h_{leg}}{A_{leg}}\left[\rho_p(T) + \rho_n(T)\right] \tag{13}$$

and

$$R_\Omega^{el} = \frac{2N\rho_{el}h_{el}}{A_{el}} \tag{14}$$

where h_{leg} and A_{leg} are the height and cross-sectional area of a copper electrode. $\rho_p(T)$, $\rho_n(T)$ and ρ_{el} are the electrical resistivity of the p-type TE leg, n-type TE leg and copper electrodes; Their values have been presented in Table 1. Through use of Eqs. (13), (14) and the results of R_Ω^{TEM} from the experiments, the ECR of the TEG module, R_E, is obtained by

$$R_E = \left(R_\Omega^{TEM} - R_\Omega^{leg} - R_\Omega^{el}\right)\frac{A_{leg}}{4N} \tag{15}$$

Here it should be pointed out that R_Ω^{TEM} and R_Ω^{leg} in the experiments were sensitive to the temperature, while R_Ω^{el}, as shown by Eq. (14), was a constant regardless of the temperature changes [27,39]. This indicates that the ECR, R_E, given by Eq. (15), is actually a temperature-dependent variable. Meanwhile, the temperatures in the TEG module slightly changed under different pressure loads . Therefore, the ECR of the TEG setup is also a function of the imposed pressure load.

So far, a set of equations, including Eqs. (10)–(12) and Eqs. (13)–(15), have been formulated. In Section 3, the TCRs at different locations and ECR of the TEG setup will be estimated by these equations with the temperature measurements (marked in Fig. 4), U-I curve by the external electronic load and materials properties in Table 1. We will investigate them using different interfacial materials and in a wide range of heat-source temperatures and pressure loads.

2.3. Uncertainty analysis on experimental measurements

In this study, the uncertainties of the experimental results were also analysed, with particular attention paid to the overall TCR and ECR. As these two key variables were calculated based on the formulas in Section 2.2, their uncertainties rely essentially on the underlying measurements contributing to their estimations. Generally, for a variable, U_R, depending on a set of independent measurments $(x_1, x_2, \ldots\ldots, x_i)$, its uncertainty, δU_R, is specified by [40,41],

$$\delta U_R = \sqrt{\left(\frac{\partial U_R}{\partial x_1}\delta x_1\right)^2 + \left(\frac{\partial U_R}{\partial x_2}\delta x_2\right)^2 + \ldots\ldots + \left(\frac{\partial U_R}{\partial x_i}\delta x_i\right)^2} \tag{16}$$

where δx_i is the instrumental error of the sensor or equipment used for the i^{th} measurment. With the help of Eq. (16), the uncertainty of the overall TCR based on Eqs. (10)–(12) is

$$\delta R_T = \sqrt{\sum_i \left(\frac{\partial R_T}{\partial T_i}\right)^2 \delta T_i^2} \tag{17}$$

where δR_T and δT_i are the uncertainties of the overall TCR, and the i^{th} involved temperature measurement, respectively. Note that the uncertainties of the component geometries and material properties are not taken into account in this analysis, as their values are directly provided from the manufacturers. As to the uncertainty of the ECR, δR_E, it is calculated based on Eqs. (15) and (16), i.e.,

$$\delta R_E = \sqrt{\left(\frac{\partial R_E}{\partial U}\right)^2 \delta U^2 + \left(\frac{\partial R_E}{\partial I}\right)^2 \delta I^2} \tag{18}$$

δU and δI are the uncertainties of the voltage and current from the electronic load.

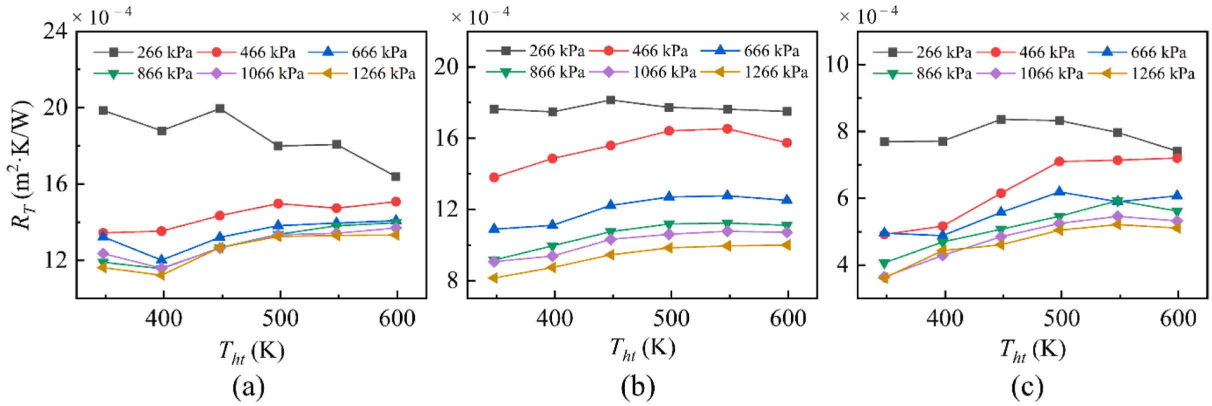

Fig. 5. Variations of the overall TCRs at different pressure loads and heat-source temperatures using (a) air, (b) graphene sheet, and (c) thermal grease.

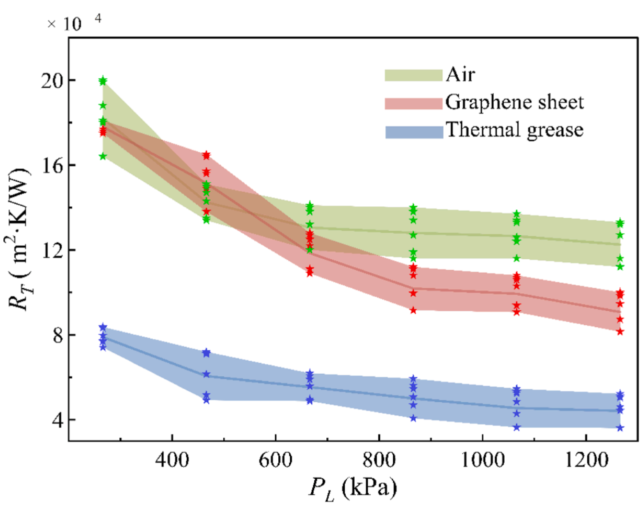

Fig. 6. The magnitude ranges of the overall TCRs with three interfacial materials. The stars in one color scattered in a vertical line represent the overall TCRs at different heat-source temperatures but one given pressure load, and with one given interfacial material (N.B.: The specific values of these temperatures can be directly read from Fig. 5).

Table 2 enumerates the uncertainties of those direct measurements, including the voltage, current and a series of temperatures at different locations. Substituting these data into Eqs. (17) and (18) results in the uncertainties of the overall TCR and ECR, which are 8.8 % and 0.19 %, respectively. It is seen that these results in our experimental study have reasonable and acceptable accuracy.

3. Experimental results and discussions

3.1. Experimental results of TCR

The TCR experiments were conducted in the TEG open-circuit mode at the water-bath temperature T_w = 293.15 K. All the temperatures at the points shown in Fig. 2(c) were measured when the imposed pressure load, P_L, varied from 266 kPa to 1266 kPa and heat-source temperature, T_{ht}, from 348.15 K to 598.15 K. In these experiments, three interfacial materials, i.e., air, graphene sheet and thermal grease, were employed on the hot and cold sides of the TEG module, respectively.

Fig. 5 (a)–5(c) show the obtained overall TCRs, using the three different interfacial materials at various pressure loads and heat-source temperatures. In the three cases, the TCR was largely reduced with the increasing pressure load. In particular, such a reduction was rather noticeable when the pressure load increased from 266 kPa to 866 kPa. We understand this is mainly because the increasing pressure load effectively squeezed out the air residue between the contacting surfaces, and thus improved the corresponding TCR.

As to the heat-source temperature, its increase led to the growth of almost all TCRs, except those at P_L = 266 kPa. Under this circumstance, the corresponding overall TCRs in the three cases first reached a peak at T_{ht} = 498.15 K, and then decreased slightly when the heat-source temperature further elevated. Note that the magnitudes of the overall TCRs were rather distinct when different interfacial materials were used. To better illustrate this feature, the overall TCRs in Fig. 5 were redrawn in Fig. 6. In the latter figure, the stars in one color represent the overall TCRs obtained with one of the three interfacial materials; Every six of them scattered in one vertical line correspond to the six heat-source temperatures but one particular pressure load used in the experiments. As just pointed out, not all the overall TCRs monotonically increased with the increasing heat-source temperature. Therefore, those stars, from bottom to top, may correspond to different heat-source temperatures at different pressure loads. Take the overall TCR at P_L = 266 kPa as an example. The heat-source temperatures of the green stars from bottom to top shown in Fig. 6 are 598.15, 498.15, 548.15, 398.15, 348.15 and 448.15 K, respectively. When the pressure load grew to P_L = 466 kPa, those heat-source temperatures (still from bottom to top) have changed to T_{ht} = 348.15, 398.15, 448.15K, 548.15, 498.15 and 598.15 K, respectively (For succinctness, we did not present the heat-source temperature corresponding to each star in Fig. 6; the specific values of these temperatures can be directly read from Fig. 5 at different pressure loads and/or with different interfacial materials). It is also seen in Fig. 6 that the overall TCR varied from 1.12×10^{-3} to 2.00×10^{-3} m²·K/W when air was the interfacial material. When it was replaced by graphene sheet or thermal grease, the magnitudes of the resulting overall TCRs fell into the range of 8.15×10^{-4} –1.81×10^{-3} m²·K/W and 3.61×10^{-4}–8.37×10^{-4} m²·K/W. In addition, the overall TCRs using thermal grease at all pressure loads were far smaller than their counterparts. As to the case of graphene sheet, the obtained TCRs at most pressure loads (except $P_L \leqslant 466$ kPa) were lower than those using air as the interfacial material. It is suggested based on the results in Fig. 6 that a large pressure load, e.g.,$P_L \geqslant 886$ kPa, should be necessarily maintained to achieve low TCR of the TEG module.

To deepen our understanding of the TCR in the TEG system, we further decomposed the overall TCR into its external and internal components, R_T^e and R_T^i. Fig. 7(a)–7(c) elaborate on their variations at different pressure loads and heat-source temperatures. It is shown that the external TCRs under all working conditions were much larger than the internal TCRs. However, both decreased with the increasing pressure load. As to the impacts of the heat-source temperature, the external TCRs, R_T^e, in the three cases grew when the heat-source temperature elevated, while the internal TCR, R_T^i, showed more complex behaviours when different interfacial materials were used. To be specific, they

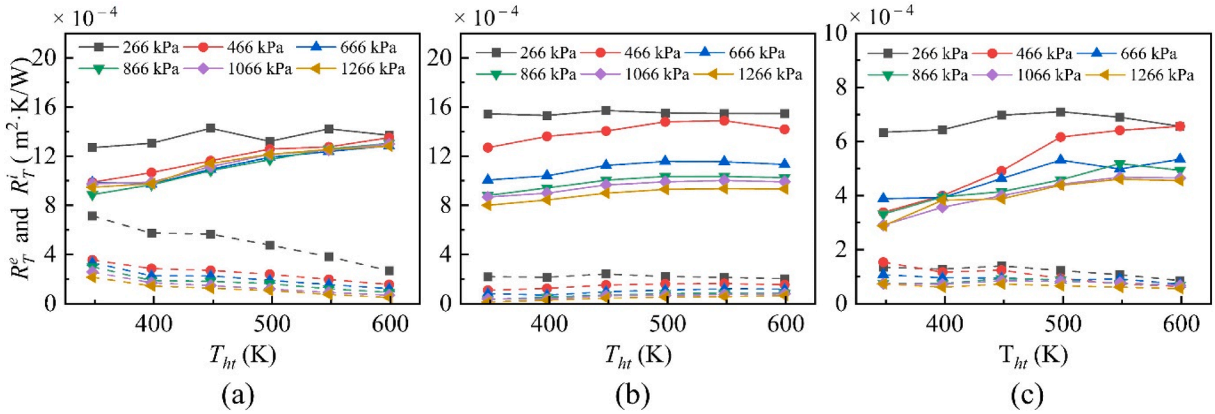

Fig. 7. Variations of the external (solid lines) and internal (dashed lines) TCRs at different pressure loads and heat-source temperatures using (a) air, (b) graphene sheet, and (c) thermal grease.

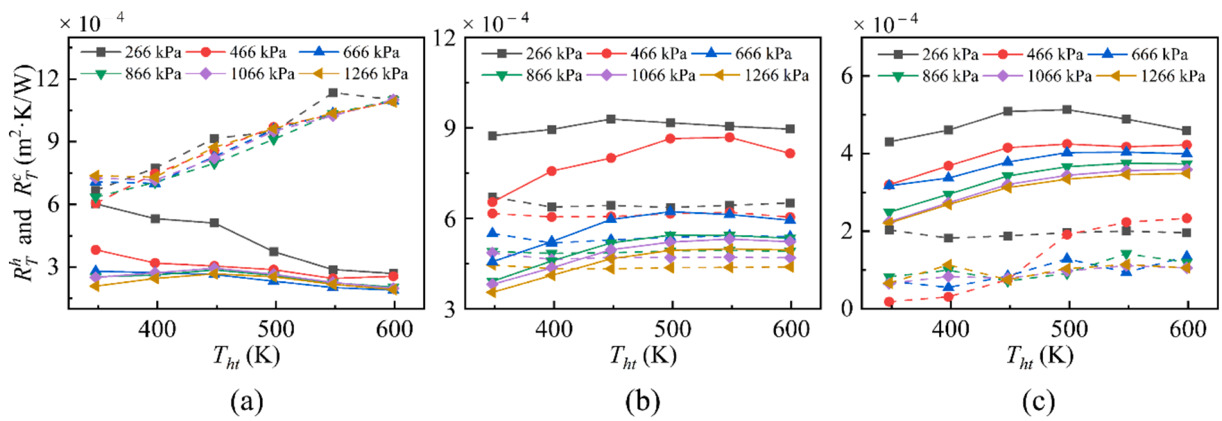

Fig. 8. Variations of the TCRs on the TEG hot (solid lines) and cold (dashed lines) sides at different pressure loads and heat-source temperatures using (a) air, (b) graphene sheet, and (c) thermal grease.

gradually decreased with the increasing heat-source temperature when air was the interfacial material. When air was replaced by either graphene sheet or thermal grease, the resulting R_T^i kept almost unchanged in a large range of the heat-source temperature. Importantly, at the same P_L and T_{ht}, the values of R_T^i in the latter two cases were much smaller than those using air. This phenomenon is attributed to the high thermal conductivity of graphene sheet and thermal grease, which could lead to more uniform temperature distributions in the horizontal direction in the experiments. Therefore, establishing uniform temperature distributions and imposing large pressure loads are two effective means to minimize the internal TCR.

It is also interesting to point out that our experiments further refined the external TCR, R_T^e, by the contributions from the hot and cold sides of the TEG module, i.e., R_T^h and R_T^c. Fig. 8(a)–8(c) exhibit the values of these two TCRs at different pressure loads and heat-source temperatures. At a given P_L and T_{ht}, the largest R_T^c and smallest R_T^h occurred when air was used. These results are of direct relevance to the surface roughness—It was 19.5 μm on the heat-sink surface contacting the cold side of the TEG module while it substantially reduced to 1.7 μm on the top surface of the aluminium block on the hot side. When graphene sheet and thermal grease were used on the cold side, both well filled into the gaps on the rough surface, and thus brought about a smaller R_T^c in comparison to that using air. On the contrary, the surface on the hot side was much smoother with smaller roughness. In this scenario, replacing air with the graphene sheet or thermal grease would cause the surface more irregular and uneven, inevitably resulting in a larger R_T^h accordingly.

So far, variations of the TCRs at different locations under different mechanical and thermal conditions were discussed. To gain a full picture of their contributions, Fig. 9 enumerates R_T^h, R_T^c and R_T^i at different heat-source temperatures and highlights their percentages in the overall TCR, R_T, with the three interfacial materials. For convenience while without loss of generality, only the results at $P_L = 1266$ kPa are presented; those obtained at the other pressure loads have similar conclusions. It is seen that R_T^i played a minor role in all cases. In particular, its percentage to R_T never exceeded 7% in the case using graphene sheet. As to R_T^c, it was a dominating component, contributing more than 60% to R_T when air was employed. What's more, such a contribution jumped to 82% at $T_{ht} = 598.15$ K. On the other hand, the major contribution to the TCR came from R_T^h in the case using thermal grease–it made around 65% contribution to R_T throughout the entire range of the heat-source temperature. The results in Fig. 9 signify the essential role of reducing the external TCR in the TEG design and optimization. Crucially, they reveal that different interfacial materials will determine on which side such a reduction is the most effective.

3.2. Experimental results of ECR

The second interest in this study is to estimate the ECR of the TEG system, which exists between the copper electrodes and TE legs. Different from the previous TCR experiments, the ECR experiments were carried out in the TEG closed-circuit mode. Under this working circumstance, an external electronic load was connected with the TEG module in series. Again, the temperature in the water bath was set $T_w = 293.15$ K, and the same pressure loads and heat-source temperatures

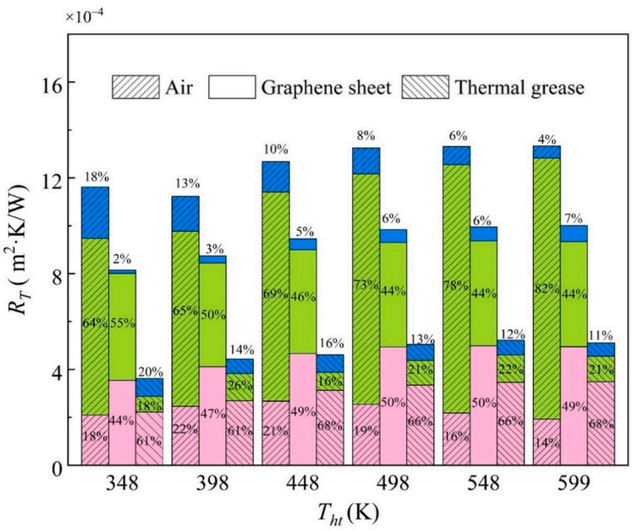

Fig. 9. The contributions of the external hot-side TCR (pink), external cold-side TCR (green) and internal TCR (blue) to the overall TCR. (For interpretation of the references to color in this figure legend, the reader is referred to the web version of this article.)

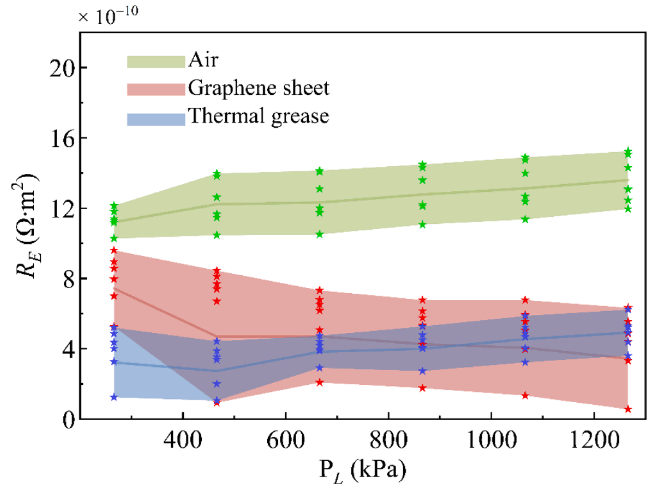

Fig. 11. The magnitude ranges of the ECRs with three interfacial materials. The stars in one color scattered in a vertical line represent the ERCs at different heat-source temperatures but one given pressure load, and with one given interfacial material (N.B.: The specific values of these temperatures can be directly read from Fig. 10).

were applied. To evaluate the overall electrical resistance of the TEG module, R_{Ω}^{TEM}, we modulated the external electronic loads from 10 Ω to 0.1 Ω at an interval of 0.1 Ω, and obtained the U-I curves by fitting the voltages and currents output by the external electronic load. With the aid of these experimental data, the magnitudes of R_E were specified based on Eqs. (13)–(15).

Fig. 10 shows the variations of the ECR, R_E, at the pressure load ranging from 266 kPa to 1266 kPa and heat-source temperature from 348.15 K to 598.15 K. Again, air, graphene sheet and thermal grease were employed as interfacial materials. It is seen that the ECR dependence on the pressure load varied with different interfacial materials. Such variation features can be explained in terms of the underlying variations of R_{Ω}^{TEM} and R_{Ω}^{leg}. To be specific, it is found that when air was used as the interfacial material, R_{Ω}^{TEM} increased but R_{Ω}^{leg} decreased with the increasing pressure load, thus leading to an increasing ECR. However, when air was replaced by graphene sheet, R_{Ω}^{TEM} decreased with the increasing pressure load. As to R_{Ω}^{leg}, it first increased when the pressure load grew. When the pressure load went beyond 666 kPa, R_{Ω}^{leg} had small drops at those larger pressure loads. It should be pointed out that although R_{Ω}^{leg} in this case presented nonmonotonic variations, its changes at the large pressure loads were insignificant. As a result, we still saw a monotone decreasing profile of R_E with the increasing P_L in Fig. 10(b). As to the case using thermal grease, R_{Ω}^{leg} slightly declined over the whole range of the pressure load, whereas R_{Ω}^{TEM} displayed a first-falling-and-then-rising profile, and had a minimum at $P_L = 466$ kPa. The compound effects of R_{Ω}^{TEM} and R_{Ω}^{leg} ultimately resulted in a decreasing R_E with the growing P_L. It is indicated from the above discussion that the dependence of R_{Ω}^{TEM} and R_{Ω}^{leg} on the pressure load is nonmonotonic and subject to the used interfacial material. More detailed investigations including both theoretical and experimental analyses will be conducted in our future study.

As to the impacts of the heat-source temperature, T_{ht}, different variations of R_E were observed with the increasing T_{ht} in the three cases using different interfacial materials. These temperature-dependent results, as shown in Fig. 10, can still be well understood in the light of the variations of R_{Ω}^{TEM} and R_{Ω}^{leg}. Generally, a larger heat-source temperature led to a larger R_{Ω}^{TEM} and R_{Ω}^{leg}. Nonetheless, their rising rates were subject to the interfacial material. Take the results using graphene sheet and thermal grease as examples. It is found that with the increasing heat-source temperature, the rise in R_{Ω}^{TEM} was always smaller than its counterpart in R_{Ω}^{leg} in both cases, resulting in a monotone decreasing R_E accordingly. As to the case using air, the rising rate of R_{Ω}^{TEM} was smaller than that of R_{Ω}^{leg} only when the growth of T_{ht} occurred after 498.15K. Before that threshold, R_{Ω}^{TEM} increased at a faster rate than R_{Ω}^{leg} did with

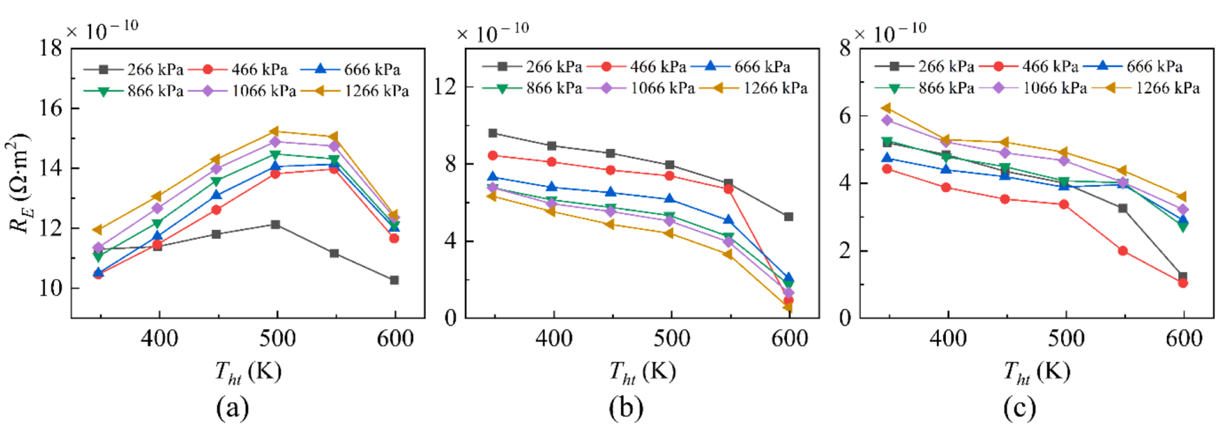

Fig. 10. Variations of the ECRs at different pressure loads and heat-source temperatures using (a) air, (b) graphene sheet, and (c) thermal grease.

the increasing T_{ht}. Therefore, it was not surprising that the non-monotonic profiles of R_E (corresponding to different pressure loads) were observed in Fig. 10(a), with the peaks at 498.15K.

Similar to the discussion on the TCRs, the magnitude ranges of the ECRs are illustrated in different colors in Fig. 11, based on the results with the three interfacial materials shown in Fig. 10. The stars in one color scattered in one single vertical line correspond to different heat-source temperatures; the specific values of these temperatures can be directly read from Fig. 10. Apparently, the experiments using air suffered from the largest ECR; it varied from 1.03×10^{-9} –1.52×10^{-9} $\Omega\cdot m^2$, far above $R_E = 5.55\times10^{-11}$ –9.60×10^{-10} $\Omega\cdot m^2$ with graphene sheet and $R_E = 1.05\times10^{-10}$ –6.23×10^{-10} $\Omega\cdot m^2$ with thermal grease in the same ranges of the pressure load and heat-source temperature. In all experiments, the minimum ECR (i.e., 5.55×10^{-11} $\Omega\cdot m^2$) was achieved at P_L = 1266 kPa and T_{ht} = 598.15 K, and using graphene sheet as the interfacial material. These results indicate that air is an unfavourable choice in terms of ECR; Replacing it by graphene sheet or thermal grease will lead to a significant reduction of the ECR of the TEG module.

3.3. Discussion of TEG performance

In this section, the performance of the TEG system in our experiment, in terms of its open-circuit voltage, V_{oc}, maximum power output, $P_{\max}$, and maximum conversion efficiency $\eta_{\max}$, was assessed with the knowledge of its TCR and ECR discussed in the previous sections. For the open-circuit voltage, it is related to the Seebeck coefficient,S, of the TE materials by [1]

$$V_{oc} = S\cdot\Delta T_0 \tag{19}$$

where ΔT_0 is the temperature difference upon the TE legs. This property, together with the maximum power output, was specified by the external electronic load. As to the maximum conversion efficiency, it is defined by

$$\eta_{\max} = \frac{P_{\max}}{q}\times 100\% \tag{20}$$

q is the heat transfer rate in the TEG module given by Eq. (9).

Fig. 12 shows the results with the three interfacial materials at different pressure loads and heat-source temperatures. It is found that V_{oc} increased with the increasing P_L, regardless of the interfacial materials in use. Its growth was approximately linear with the increasing T_{ht} as shown in Fig. 12(a)–12(c). When these two external working conditions were set, the values of V_{oc} in the experiments using thermal grease were always larger than their counterparts with air and graphene sheet. The underlying cause is mainly because thermal grease yielded low TCR, thereby resulting in a higher temperature difference upon the TE legs.

For the maximum power output, $P_{\max}$, large T_{ht} and P_L exerted positive impacts on its enhancement. As shown in Fig. 12(d)–12(f), $P_{\max}$ in all cases increased with the rises of T_{ht} and P_L. To be similar to the variations of V_{oc}, the values of $P_{\max}$ in the case using thermal grease were much larger than those with graphene sheet and air. For example, $P_{\max}$ = 9.03 W at P_L = 1266 kPa and T_{ht} = 598.15 K with thermal grease, which was higher by 83% than its counterpart with air. Such an enhancement resulted from the compounding effects of the lower TCR and ECR of the TEG system using thermal grease. Under these circumstances, the lower TCR gave rise to a larger ΔT_0, while the lower ECR led to a smaller R_Ω^{TEM}. Both contributed to the improvement of $P_{\max}$, as given by Eq. (2).

Fig. 12(h)–12(j) also show the maximum conversion efficiency of the TEG system, $\eta_{\max}$, working at different pressure loads and heat-source temperatures with the three interfacial materials. Generally speaking, the larger T_{ht} was provided, the higher $\eta_{\max}$ the TEG system delivered. As to the pressure load, its impacts on $\eta_{\max}$ varied with different interfacial materials. For example, in the cases using air and thermal grease, $\eta_{\max}$ first had a rapid rise when the pressure load changed from 266 kPa to 466 kPa. It then remained almost unchanged when the pressure load continued increasing to even those high values. Nevertheless, the growth of $\eta_{\max}$ in the experiments using graphene sheet gradually slowed down with the increasing pressure load over its entire range. It is also interesting to point out that the best $\eta_{\max}$ was obtained in the experiment using thermal grease at P_L = 1266 kPa and T_{ht} = 598.15 K. It was $\eta_{\max}$ = 6.9%, larger by 42% and 18% than that with air and graphene sheet at the same P_L and T_{ht}. Again, this phenomenon is attributed to the low TCR and ECR of the TEG system using thermal grease, as discussed in sections 3.1 and 3.2.

At this stage, it is concluded that low TCR will increase the temperature difference upon the TE legs, and thus facilitate the TEG a higher open-circuit voltage. Furthermore, this favourable factor, together with low ECR, will also lead to a higher maximum power output and better maximum conversion efficiency of the TEG. It is implied in future TEG design that we should select appropriate interfacial materials, and optimize the thermal settings and mechanical conditions to regulate the magnitudes of both TCR and ECR as small as possible.

4. ANN model for TCR of the TEG system

So far, a series of experiments have been conducted to specify the TCR and ECR of the TEG system and their contributions to the TEG performance. In particular, it is found that TCR depends on a variety of parameters, including the interfacial materials used on the hot and cold sides of the TEG module, imposed pressure load, and heat-source temperature. It has to be admitted, on the other hand, that although the total number of experiments in this study has been more than 100, the experimental results discussed in previous sections indeed only cover a small portion of the working conditions. For example, the values of TCR are unknown yet when the heat-source temperature or pressure load deviates from the given experimental settings. Moreover, the conventional empirical correlation is found ineffective as the TEG system involves multiple contributing factors to its TCR, and their impacts are nonlinear. Bearing these challenges in mind, we strive to make a paradigm shift from the conventional experimental methodology to machine learning in this section. To tackle the nonlinear dependence of TCR on those external conditions, an artificial neural networks (ANN) model, which excels in dealing with multi-parameter nonlinear problems, is developed based on the experimental data. It will be shown that the proposed ANN model can facilitate accurate and cost-effective prediction of TCR for a TEG operating in various working conditions.

4.1. ANN model for TCR

To be specific, we focus on a fully-connected ANN model based on the backpropagation learning algorithm, which is mainly characterised by the input variables, number of hidden layers, numbers of nodes (neurons) and activation functions in each layer, and training algorithm [42]. In this study, the type of the used interfacial materials, imposed pressure load, P_L, temperature on the top surface of aluminium block contacting the TEG module, T_h, and temperature of the heat sink, T_c, were chosen as the input variables. The ANN model only included one hidden layer, because for the problem under investigation including more hidden layers did not bring about substantial improvements in its results. As to the output layer, the overall TCR was set as the output of our interest. In so doing, an ANN model with a three-layer algorithmic structure is shown in Fig. 13.

In modelling, all the experimental TCR data with the three interfacial materials were first collected to form a total dataset. They were randomly divided into three subsets, i.e., the training set (70 % data),

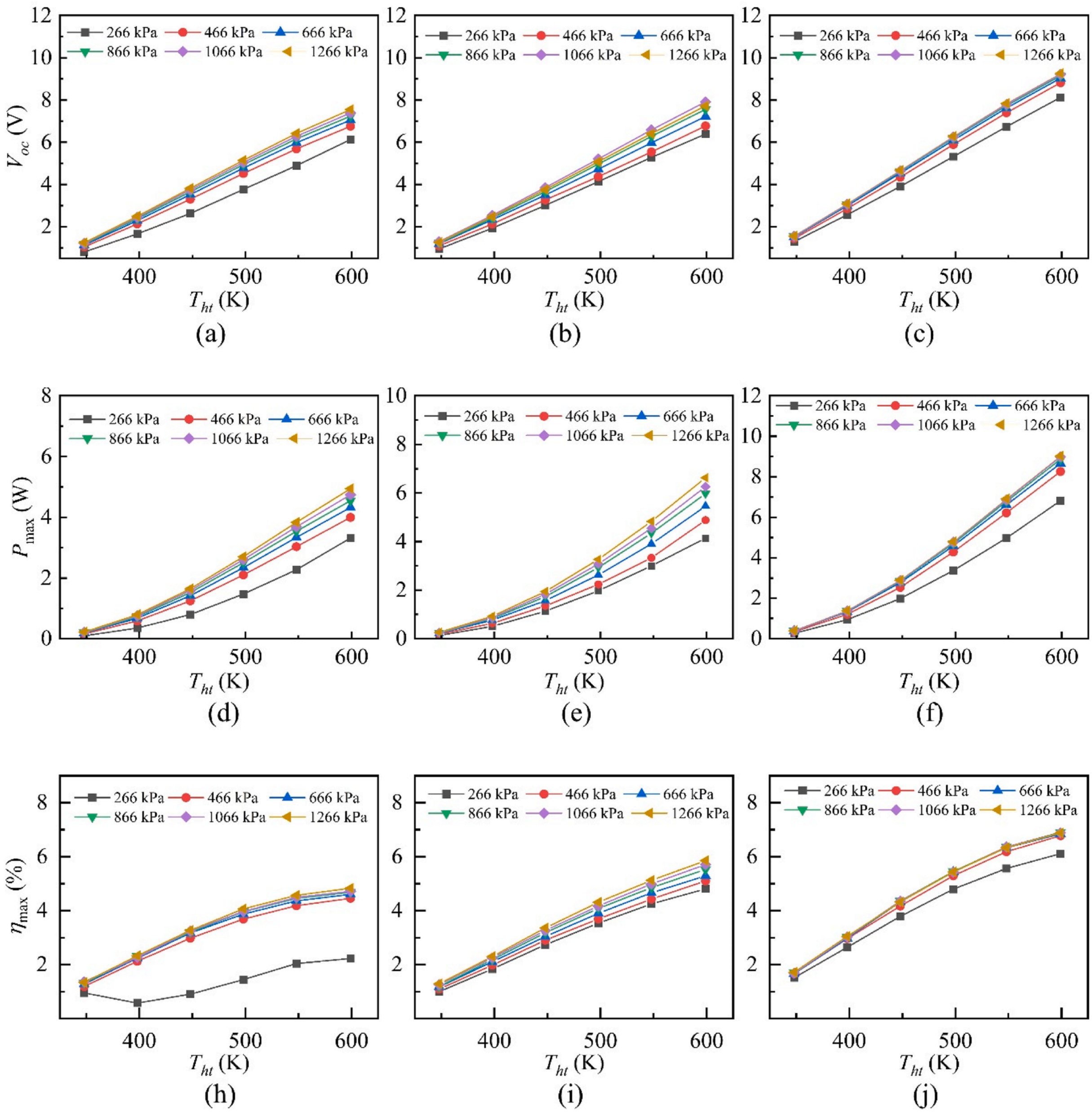

Fig. 12. The open-circuit voltages (a)–(c), maximum power outputs (d)–(f), and maximum conversion efficiency (h)–(j) of the TEG system using air (a) (d) (h), graphene sheet (b) (e) (i), and thermal grease (c) (f) (j) as its interfacial materials.

validation set (15 % data) and testing set (15 % data). The material type for air, graphene sheet and thermal grease in the ANN model was represented by the material indices “1”, “2” and “3”, respectively. T_h is defined by

$$T_h = T_I - qR_I \tag{21}$$

where T_I is the average temperature of layer I in the aluminium block. R_I and q represent the thermal resistance between layer I and the top surface of the aluminium block contacting the TEG module, and the heat transfer rate flowing into the TEG module, respectively. Note that in the hidden and output layers, we associated their inputs, **x**, with their outputs, **y**, by [43]

$$\mathbf{y} = f_i(\mathbf{wx} + \mathbf{b}),\ i = o, h \tag{22}$$

where the activation function in the output layer was $f_o(\mathbf{x}) = \mathbf{x}$, and it was formulated as a sigmoidal symmetric function in the hidden layer,

$$f_h(\mathbf{x}) = \frac{2}{1 + e^{-2\mathbf{x}}} - 1 \tag{23}$$

In Eq. (22), **w** and **b** are the corresponding weight and bias specified by the Levenberg-Marquardt Backpropagation algorithm [44]. Its basic iteration is

$$\Lambda_{k+1} = \Lambda_k - \left[\mathbf{J}^{\mathrm{T}}(\Lambda_k)\mathbf{J}(\Lambda_k) + \mu\mathbf{I}\right]^{-1}\mathbf{J}^{\mathrm{T}}(\Lambda_k)\left(\mathbf{y}_{pre} - \mathbf{y}_{exp}\right)(\Lambda_k) \tag{24}$$

where Λ_k represents the results of the k^{th} iteration and $\mathbf{J}(\Lambda_k)$ is the Jacobian matrix [45]. **I** is a unit matrix and μ is a positive constant. It is worth mentioning that to better assess its accuracy, four criteria were introduced in the ANN model, i.e., the mean square error (*MSE*), correlation coefficient (*r*), mean absolute deviation (*AAD*), and relative deviation (*RD*). They are defined as follows [42,46]

$$MSE = \frac{1}{n}\left(\mathbf{y}_{pre} - \mathbf{y}_{exp}\right)^{\mathrm{T}}\left(\mathbf{y}_{pre} - \mathbf{y}_{exp}\right) \tag{25}$$

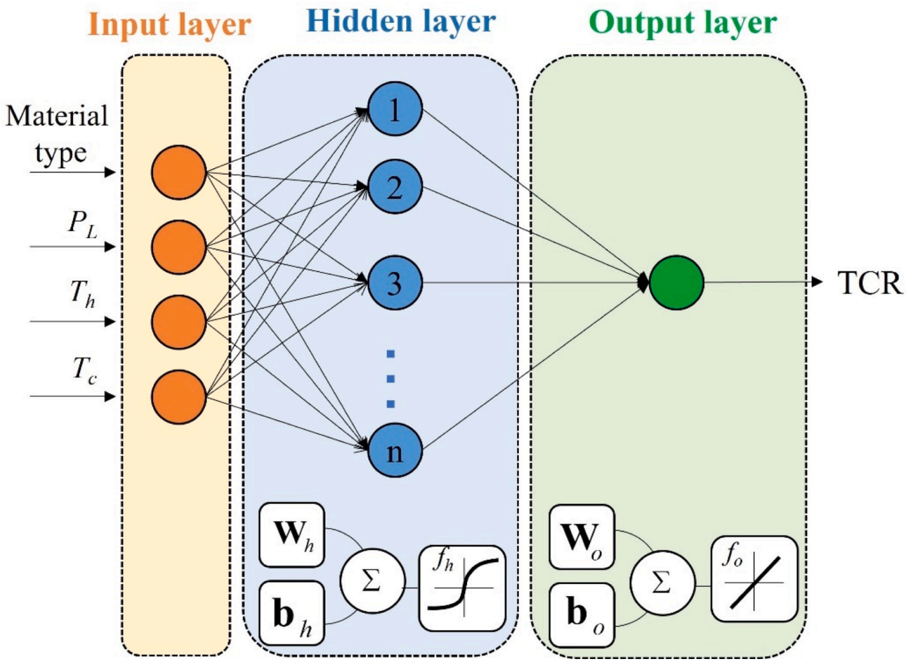

Fig. 13. The three-layer algorithmic structure of the ANN model for TCR prediction.

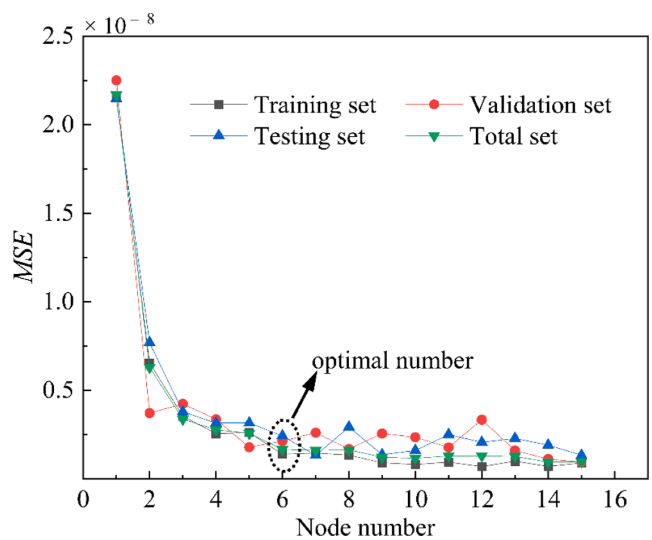

Fig. 14. The values of *MSE* at different node numbers in the hidden layer.

$$r = \frac{C_{cov}(\mathbf{y}_{pre}, \mathbf{y}_{exp})}{\sqrt{C_{cov}(\mathbf{y}_{pre}, \mathbf{y}_{exp})}\sqrt{C_{cov}(\mathbf{y}_{pre}, \mathbf{y}_{exp})}} \tag{26}$$

$$AAD = \frac{1}{n}\sum_{i=1}^{n}\left|\frac{y_{pre}^{i} - y_{exp}^{i}}{y_{exp}^{i}}\right| \times 100\% \tag{27}$$

$$RD = \frac{y_{pre}^{i} - y_{exp}^{i}}{y_{exp}^{i}} \times 100\% \tag{28}$$

where the subscript i represents the i^{th} component of a vector, and C_{cov} is the covariance.

To achieve a reasonable balance between computational accuracy and efficiency, the node number in the hidden layer of our ANN model was also optimized by the trial-and-error method using *MSE* as the objective function. Fig. 14 shows the resulting *MSE*s when the node number was increased from 1 to 15. It is plain that *MSE* decreased with the increasing node number. In particular, when the node number grew up to 6 and beyond, it almost converged, only with minor fluctuations. In the light of these results, we therefore allocated 6 nodes in the hidden layer in the ANN model in this study, together with 4 nodes in its input layer and 1 in its output layer.

Table 4
MSE, *r* and *ADD* of the ANN model based on different datasets.

Datasets	*MSE*	*r*	*AAD*
Training	2.47×10^{-9}	0.99455	2.89%
Validation	2.46×10^{-9}	0.99324	3.50%
Testing	1.71×10^{-9}	0.99348	4.22%
Total	2.36×10^{-9}	0.99421	3.18%

Table 3
The weights and biases in the hidden and output layers of the ANN model.

Node No.	$\mathbf{w}_h$				$\mathbf{b}_h$	$\mathbf{w}_o$	$\mathbf{b}_o$
	Material type	P_L	T_h	T_c			
1	0.4192	2.4037	−0.7062	1.8334	2.6945	−0.3244	0.4893
2	−2.3671	−0.3850	0.1280	−1.0369	−0.1921	0.4551	
3	−0.0951	−2.6165	0.9904	0.2641	−1.6007	0.0739	
4	0.0569	−0.3233	1.4217	0.0040	0.7364	0.1497	
5	−0.3057	−2.8978	−1.2526	1.2630	−3.7371	0.5030	
6	−1.7859	0.7929	1.4205	0.1292	−2.2447	0.0517	

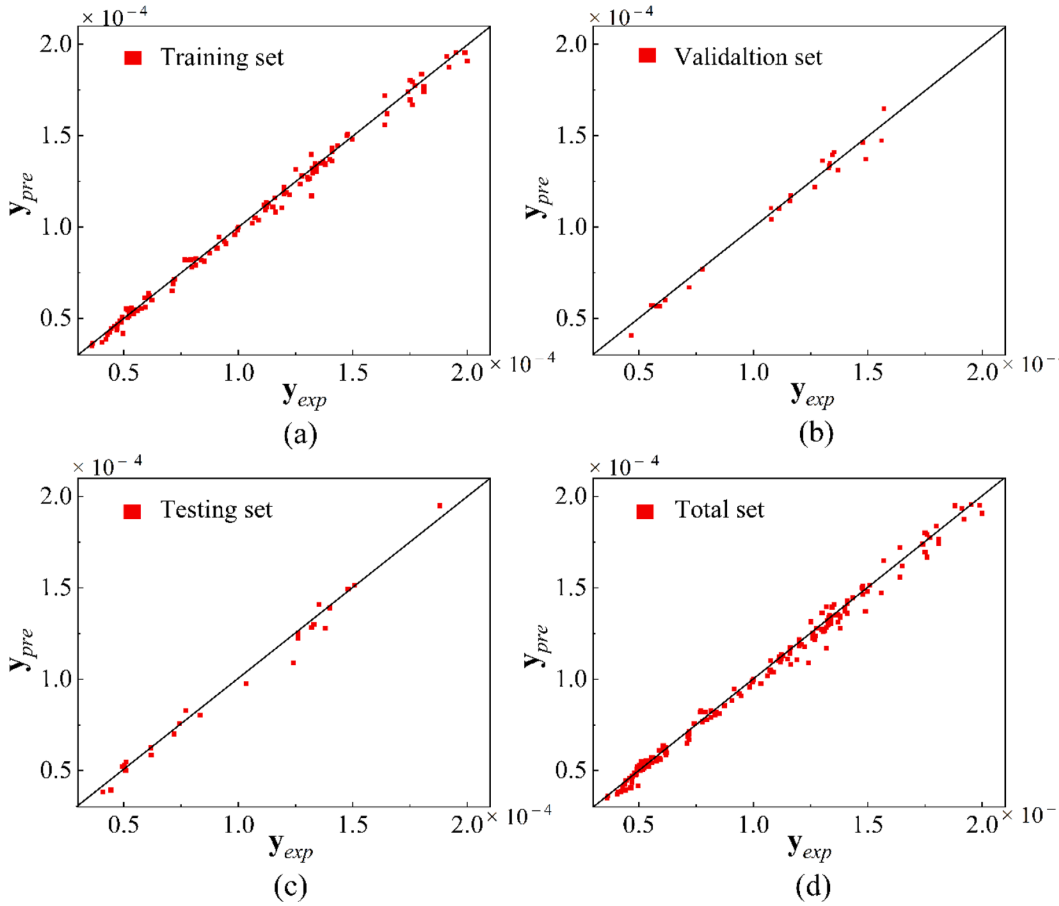

Fig. 15. Parity plots of ANN predictions versus experimental data in (a) training set, (b) validation set, (c) testing set and (d) total set.

4.2. ANN results and discussion

The proposed ANN model was optimized to estimate the overall TCR based on the training, validation, testing and total sets. Table 3 presents the optimized weights and biases in the activation functions in the hidden and output layers, respectively.

Through use of these weights and biases, the resulting values of *MSE*, *r* and *ADD* for different datasets are summarized in Table 4. It is seen that under the current ANN modelling settings, *MSEs* of the different data sets were 2.47×10^{-9} (training set), 2.46×10^{-9} (validation set), 1.71×10^{-9} (test set), and 2.36×10^{-9} (total set); The variations of the correlation coefficients, *r*, were limited to 99.32% −99.46%. As to *AAD,* its values for the four datasets were not beyond 4.5%.

Furthermore, Fig. 15(a)–15(d) show the parity plots comparing the experimental data in the four datasets to the corresponding TCR predictions by the ANN model. For convenience, the solid diagonals were drawn as benchmarks. It is found TCR predictions by the proposed ANN model were in good agreement with the experimental data in the four datasets−All the points, $\left(\mathbf{y}_{exp}, \mathbf{y}_{pre}\right)$, were distributed within a narrow vicinity along the diagonals. In addition, Fig. 16(a)–16(c) also illustrate the obtained relative deviations, *RDs*, with different interfacial materials, pressure loads, P_L, and temperatures on the top surface of aluminium block, T_h. It is shown that the vast majority (about 94.6 %) of the ANN predictions deviated from the experimental data in a rather small range, i.e., $RD \leqslant \pm 5\%$. In particular, among the three used interfacial materials, the ANN model gave the best prediction for TEG with graphene sheet, and its prediction became more accurate when T_h elevated beyond 400 K. As to P_L, Fig. 16(b) showed that the prediction accuracy of the proposed ANN model did not have substantial variations at different pressure loads.

In summary, the results in Table 4, Figs. 15 and 16 have clearly demonstrated that the proposed ANN model can achieve satisfactory accuracy for predicting the overall TCR of a TEG. It can be used as a reliable and cost-effective tool for TCR prediction in future TEG optimization.

5. Conclusion

TCR and ECR are two important factors affecting the temperature difference upon the TE legs and the electrical resistance of the TEG module. Therefore, their precise estimations are of direct relevance to the TEG design, optimization and performance. In this study, experiments and detailed thermal and electric analyses on a TEG system were performed. Based on the obtained experimental data, the overall TCR, external hot- and cold-side TCR, TCR inside the TEG module, and ECR have been systematically specified using different interfacial materials at various heat-source temperatures and pressure loads. Significantly, an ANN model was proposed based on the experimental results. This facilitates TCR prediction in a cost-effective manner for future TEG design and optimization. In this section, some salient conclusions are drawn as follows:

(1) Generally, small overall TCR can be obtained at a large pressure load and a low heat-source temperature. Its magnitudes also directly depend on the interfacial materials used in the TEG system. In this article, R_T with air, graphene sheet and thermal grease were found in the range of $(1.12 - 2.00) \times 10^{-3}$ m^2·K/W,

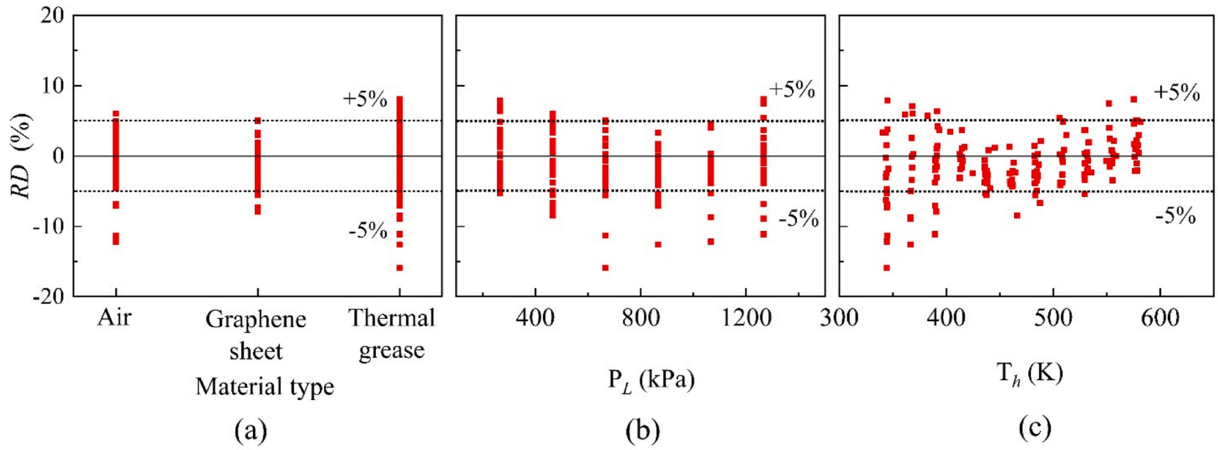

Fig. 16. Relative deviations between the ANN predictions and experimental data with different (a) interfacial materials; (b) pressure loads, P_L; (c) temperatures on the top surface of aluminium block, T_h.

$(0.82-1.81)\times 10^{-3}$ m²·K/W, and $(3.61-8.37)\times 10^{-4}$ m²·K/W, respectively. In particular, the lowest overall TCR,$R_T = 3.61\times 10^{-4}$ m²·K/W, was obtained at $P_L = 1266$ kPa and $T_{ht} = 348.15$ K when thermal grease was used. These results indicate that for a TEG operating at a high heat-source temperature, choosing thermal grease as interfacial material and imposing relatively larger pressure loads ($P_L \geqslant 866$ kPa) can effectively reduce its TCR.

(2) The experimental study in this article further revealed that the external TCR contributed more than 80% to the overall TCR, which was far beyond its internal counterpart. Therefore, one of focuses in TEG optimization should be on reducing its external TCR.

(3) Particular care should also be paid to surface roughness, whose effects on TCR were clarified in our analyses on the hot and cold-side TCRs of the TEG module in Section 3.1. It is seen that for a rough interface (which is on the cold side), thermal grease helped to fill in the gap and hence resulted in low TCR. This is contrary to the smooth interface on the hot side. In the latter case, the use of thermal grease led to deterioration in thermal contact.

(4) As to ECR, its magnitudes in our experiments varied from 1.03×10^{-9} to 1.52×10^{-9} Ω·m² using air, 0.56×10^{-10} to 9.60×10^{-10} Ω·m² using graphene sheet and 1.05×10^{-10} to 6.23×10^{-10} Ω·m² using thermal grease as the interfacial material. In particular, it is found that low values of ECR in the case of thermal grease were obtained at high heat-source temperatures and small pressure loads, (e.g., $P_L = 466$ kPa). These are different from the conditions for low TCR as discussed in Point 1. It is indicated that there are no simple compatible working conditions for a TEG operation, under which both the smallest TCR and ECR can be obtained at the same time.

(5) In a more comprehensive sense, the performance of the TEG system was assessed in terms of its open-circuit voltage, maximum power output and maximum conversion efficiency. The best performance was achieved at $P_L = 1266$ kPa, $T_{ht} = 598.15$ K with thermal grease as the interfacial material, in which $V_{oc} = 9.26$ V, $P_{\max} = 9.03$ W and $\eta_{\max} = 6.9\%$. They were larger by 23%, 83%, and 42% than those with air, respectively. All the results demonstrate that through combinations of appropriate working conditions, including the heat-source temperature, pressure load and interfacial material, TCR and ECR of a TEG can be regulated at relatively low values (although not the smallest), and the TEG can achieve good performance.

(6) In addition to those aforementioned experimental findings, an ANN model for TCR prediction of the TEG system was developed. The numerical results presented satisfactory accuracy, with $MSE = 2.36\times 10^{-9}$, $r = 99.4\%$, and $AAD = 3.18\%$. Our study in this article indicates the ANN method could be a promising and reliable tool for TCR predictions in future TEG design and optimization.

Declaration of Competing Interest

The authors declare that they have no known competing financial interests or personal relationships that could have appeared to influence the work reported in this paper.

Data availability

Data will be made available on request.

Acknowledgments

The authors are grateful for the financial support from the Ningbo Science and Technology Bureau's Technology Project under Grant No. 2019B10042. Ying Li acknowledges the financial support from China Scholarship Council (CSC). Yong Shi also acknowledges the partial financial support from Ningbo Key Laboratory on Energy Material and Technology.

Appendix A. The electrical resistances of the TEG module under different experimental conditions

In this appendix, the electrical resistances of the TEG module, R_{Ω}^{TEM}, obtained by the U-I curve fitting under different experimental conditions were presented. For different interfacial materials, the corresponding electrical resistances are given by Tables A1–A3, respectively.

Table A1
R_{Ω}^{TEM} with air as the interfacial material.

T_{ht} (K)	P_L (kPa)					
	266	466	666	866	1026	1266
348.15	1.74109	1.71544	1.71728	1.73043	1.73731	1.75381
398.15	1.96235	1.96083	1.96079	1.97199	1.97958	1.99254
448.15	2.1949	2.21206	2.21841	2.22659	2.23113	2.24477
498.15	2.43924	2.47333	2.47851	2.48324	2.48713	2.49623
548.15	2.67889	2.72349	2.72925	2.73338	2.7307	2.73809
598.15	2.91182	2.92283	2.93869	2.94194	2.93704	2.93805

Table A2
R_{Ω}^{TEM} with graphene sheet as the interfacial material.

T_{ht} (K)	P_L (kPa)					
	266	466	666	866	1026	1266
348.15	1.66565	1.63468	1.60983	1.59311	1.59489	1.58293
398.15	1.82724	1.80092	1.77555	1.75907	1.75459	1.74275
448.15	1.99399	1.96625	1.94676	1.92792	1.92296	1.90329
498.15	2.15441	2.13055	2.11688	2.09664	2.08843	2.06857
548.15	2.3121	2.29304	2.27741	2.25484	2.24374	2.22398
598.15	2.45287	2.3522	2.39355	2.3831	2.36704	2.34226

Table A3
R_{Ω}^{TEM} with thermal grease as the interfacial material.

T_{ht} (K)	P_L (kPa)					
	266	466	666	866	1026	1266
348.15	1.57405	1.52739	1.52828	1.54371	1.5569	1.56685
398.15	1.75906	1.69113	1.68895	1.70207	1.71403	1.72024
448.15	1.93563	1.85783	1.85577	1.86715	1.87456	1.88215
498.15	2.11774	2.02874	2.02519	2.03361	2.04033	2.04852
548.15	2.29666	2.19875	2.19227	2.19766	2.20128	2.21172
598.15	2.43637	2.35607	2.35243	2.35244	2.35371	2.36357

References

[1] D.M. Rowe, Thermoelectrics Handbook, CRC Press, 2005.
[2] M.S. El-Genk, H.H. Saber, T. Caillat, Efficient segmented thermoelectric unicouples for space power applications, Energ Convers. Manage. 44 (2003) 1755–1772.
[3] R.C. O'Brien, R.M. Ambrosi, N.P. Bannister, S.D. Howe, H.V. Atkinson, Safe radioisotope thermoelectric generators and heat sources for space applications, J. Nucl. Mater. 377 (2008) 506–521.
[4] F. Suarez, A. Nozariasbmarz, D. Vashaee, M.C. Öztürk, Designing thermoelectric generators for self-powered wearable electronics, Energ. Environ. Sci. 9 (2016) 299–2113.
[5] W. Zeng, X. Tao, S. Lin, C. Lee, D. Shi, K. Lam, et al., Defect-engineered reduced graphene oxide sheets with high electric conductivity and controlled thermal conductivity for soft and flexible wearable thermoelectric generators, Nano Energy 54 (2018) 163–174.
[6] S. Khanmohammadi, M.M. Baseri, P. Ahmadi, A.A.A.A. Al-Rashed, M. Afrand, Proposal of a novel integrated ocean thermal energy conversion system with flat plate solar collectors and thermoelectric generators: Energy, exergy and environmental analyses, J. Clean. Prod. 256 (2020), 120600.
[7] M.Z. Malik, F. Musharavati, S. Khanmohammadi, M.M. Baseri, P. Ahmadi, D. D. Nguyen, Ocean thermal energy conversion (OTEC) system boosted with solar energy and TEG based on exergy and exergo-environment analysis and multi-objective optimization, Sol. Energy 208 (2020) 559–572.
[8] A. Riahi, A. Ben Haj Ali, A. Fadhel, A. Guizani, M. Balghouthi, Performance investigation of a concentrating photovoltaic thermal hybrid solar system combined with thermoelectric generators, Energ Convers. Manage. 205 (2020), 112377.
[9] S. Shittu, G. Li, Q. Xuan, X. Xiao, X. Zhao, X. Ma, et al., Transient and non-uniform heat flux effect on solar thermoelectric generator with phase change material, Appl. Therm. Eng. 173 (2020), 115206.
[10] D. Kraemer, B. Poudel, H. Feng, J.C. Caylor, B. Yu, X. Yan, et al., High-performance flat-panel solar thermoelectric generators with high thermal concentration, Nat. Mater. 10 (2011) 532–538.
[11] G. Li, Y. Zheng, J. Hu, W. Guo, Experiments and a simplified theoretical model for a water-cooled, stove-powered thermoelectric generator, Energy 185 (2019) 437–448.
[12] X.F. Zheng, C.X. Liu, R. Boukhanouf, Y.Y. Yan, W.Z. Li, Experimental study of a domestic thermoelectric cogeneration system, Appl. Therm. Eng. 62 (2014) 69–79.
[13] K. Huang, B. Li, Y. Yan, Y. Li, S. Twaha, J. Zhu, A comprehensive study on a novel concentric cylindrical thermoelectric power generation system, Appl. Therm. Eng. 117 (2017) 501–510.
[14] B. Li, K. Huang, Y. Yan, Y. Li, S. Twaha, J. Zhu, Heat transfer enhancement of a modularised thermoelectric power generator for passenger vehicles, Appl Energ. 205 (2017) 868–879.
[15] A. Narjis, C.T. Liang, H. El Aakib, A. Tchenka, A. Outzourhit, Design optimization for maximized thermoelectric generator performance, J. Electron. Mater. 49 (2020) 306–310.
[16] R. Rodriguez, M. Preindl, J.S. Cotton, A. Emadi, Review and trends of thermoelectric generator heat recovery in automotive applications, IEEE T. Veh. Technol. 68 (2019) 5366–5378.
[17] W. Ren, Q. Song, H. Zhu, J. Mao, L. You, G.A. Gamage, et al., Intermediate-level doping strategy to simultaneously optimize power factor and phonon thermal conductivity for improving thermoelectric figure of merit, Mater. Today Phys. 15 (2020), 100250.
[18] J. Wang, B. Zhang, H. Kang, Y. Li, X. Yaer, J. Li, et al., Record high thermoelectric performance in bulk $SrTiO_3$ via nano-scale modulation doping, Nano Energy 35 (2017) 387–395.
[19] K.S. Kim, Y.M. Kim, H. Mun, J. Kim, J. Park, A.Y. Borisevich, et al., Direct observation of inherent atomic-scale defect disorders responsible for high-performance Ti_{1-x} Hf_x $NiSn_{1-y}$ Sb_y Half-Heusler thermoelectric alloys, Adv. Mater. (2017) 29.
[20] E. Skoug, C. Zhou, Y. Pei, D.T. Morelli, High thermoelectric power factor in alloys based on CoSi, Appl. Phys. Lett. 94 (2009) 22115.
[21] O.R. Fitriani, B.D. Long, M.C. Barma, M. Riaz, M.F.M. Sabri, et al., A review on nanostructures of high-temperature thermoelectric materials for waste heat recovery, Renew. Sust. Energ Rev. 64 (2016) 635–659.
[22] M.F. Remeli, A. Date, B. Orr, L.C. Ding, B. Singh, N.D.N. Affandi, et al., Experimental investigation of combined heat recovery and power generation using a heat pipe assisted thermoelectric generator system, Energ Convers. Manage. 111 (2016) 147–157.
[23] K.S. Garud, J. Seo, M.S. Patil, Y. Bang, Y. Pyo, C. Cho, et al., Thermal–electrical–structural performances of hot heat exchanger with different internal fins of thermoelectric generator for low power generation application, J. Therm. Anal. Calorim. 143 (2021) 387–419.
[24] F.P. Brito, J. Martins, E. Hançer, N. Antunes, L.M. Gonçalves, Thermoelectric exhaust heat recovery with heat pipe-based thermal control, J. Electron. Mater. 44 (2015) 1984–1997.
[25] Q. Tan, G. Chen, Y. Sun, B. Duan, G. Li, P. Zhai, Performance of annular thermoelectric couples by simultaneously considering interface layers and boundary conditions, Appl. Therm. Eng. 174 (2020), 115301.
[26] A.B. Zhang, B.L. Wang, D.D. Pang, L.W. He, J. Lou, J. Wang, et al., Effects of interface layers on the performance of annular thermoelectric generators, Energy 147 (2018) 612–620.
[27] C.N. Kim, Development of a numerical method for the performance analysis of thermoelectric generators with thermal and electric contact resistance, Appl. Therm. Eng. 130 (2018) 408–417.
[28] A.B. Zhang, B.L. Wang, D.D. Pang, J.B. Chen, J. Wang, J.K. Du, Influence of leg geometry configuration and contact resistance on the performance of annular thermoelectric generators, Energ Convers. Manage. 166 (2018) 337–342.
[29] T. Sakamoto, T. Iida, T. Sekiguchi, Y. Taguchi, N. Hirayama, K. Nishio, et al., Selection and evaluation of thermal interface materials for reduction of the thermal contact resistance of thermoelectric generators, J. Electron. Mater. 43 (2014) 3792–3800.
[30] S. Wang, T. Xie, H. Xie, Experimental study of the effects of the thermal contact resistance on the performance of thermoelectric generator, Appl. Therm. Eng. 130 (2018) 847–853.
[31] Y. Li, W. Zhu, D. Luo, Y. Shi, Y. Ren, X. Wang, et al., Experimental study on thermal contact resistance of thermoelectric generators, AIP Conf. Proc. 2681 (2022).
[32] R. Buchalik, G. Nowak, I. Nowak, Mathematical model of a thermoelectric system based on steady- and rapid-state measurements, Appl Energ. 293 (2021), 116943.
[33] B. Beltrán-Pitarch, F. Vidan, J. García-Cañadas, Thermal contact resistance evaluation of a thermoelectric system by means of three I-V curves, Int. J. Heat Mass Tran. 173 (2021), 121247.
[34] B. Beltrán-Pitarch, J. Maassen, J. García-Cañadas, Comprehensive impedance spectroscopy equivalent circuit of a thermoelectric device which includes the internal thermal contact resistances, Appl Energ. 299 (2021), 117287.
[35] Y. Kim, G. Yoon, S.H. Park, Direct Contact Resistance Evaluation of Thermoelectric Legs, Exp. Mech. 56 (2016) 861–869.
[36] Aluminum 6061-T6 (UNS AA96061). https://www.nist.gov/mml/acmd/aluminum-6061-t6-uns-aa96061.
[37] Electrolytic tough pitch (ETP) copper, UNS C11000, H00 temper flat products. http://www.matweb.com/search/DataSheet.aspx?MatGUID=3c78d450e90f48c48d68e2d17a8e51f7.
[38] Alumina, alpha Al_2O_3, 96%. http://www.matweb.com/search/datasheet.aspx?MatGUID= a8b34afe799742b4ad3b8642fa0be65d.
[39] T. Yin, Z. Li, P. Peng, W. Liu, Y. Shao, Z. He, Performance analysis of a novel Two-stage automobile thermoelectric generator with the Temperature-dependent materials, Appl. Therm. Eng. 195 (2021), 117249.
[40] R.J. Moffat, Describing the Uncertainties in Experimental Results, Exp. Therm. Fluid Sec. 1 (1988) 3–17.
[41] R.J. Moffat, Using Uncertainty Analysis in the Planning of an Experiment, ASME. J. Fluids Eng. 107 (1985) 173–178.

[42] N. Gao, X. Wang, Y. Xuan, G. Chen, An artificial neural network for the residual isobaric heat capacity of liquid HFC and HFO refrigerants, Int. J. Refrig 98 (2019) 381–387.
[43] X. Wang, B. Li, Y. Yan, N. Gao, G. Chen, Predicting of thermal resistances of closed vertical meandering pulsating heat pipe using artificial neural network model, Appl. Therm. Eng. 149 (2019) 1134–1141.
[44] Z. Ye, M.K. Kim, Predicting electricity consumption in a building using an optimized back-propagation and Levenberg–Marquardt back-propagation neural network: Case study of a shopping mall in China, Sustain. Cities Soc. 42 (2018) 176–183.
[45] J. Bilski, B. Kowalczyk, A. Marchlewska, J.M. Zurada, Local Levenberg-Marquardt Algorithm for Learning Feedforwad Neural Networks, J. Artif. Intell. Soft Comput. Res. 10 (2020) 299–316.
[46] X. Wang, Y. Yan, X. Meng, G. Chen, A general method to predict the performance of closed pulsating heat pipe by artificial neural network, Appl. Therm. Eng. 157 (2019), 113761.